

# A Generalized Method for the Analysis of Planar Biaxial Mechanical Data Using Tethered Testing Configurations

**Will Zhang**

Department of Biomedical Engineering,  
Center for Cardiovascular Simulation,  
Institute for Computational Engineering and Sciences,  
The University of Texas at Austin,  
Austin, TX 78712-1229

**Yuan Feng<sup>1</sup>**

Department of Biomedical Engineering,  
Center for Cardiovascular Simulation,  
Institute for Computational Engineering and Sciences,  
The University of Texas at Austin,  
Austin, TX 78712-1229

**Chung-Hao Lee**

Department of Biomedical Engineering,  
Center for Cardiovascular Simulation,  
Institute for Computational Engineering and Sciences,  
The University of Texas at Austin,  
Austin, TX 78712-1229

**Kristen L. Billiar**

Department of Biomedical Engineering,  
Worcester Polytechnic Institute,  
Worcester, MA 01609-2280

**Michael S. Sacks<sup>2</sup>**

W. A. "Tex" Moncrief, Jr. Simulation-Based  
Engineering Science Chair I,  
Professor of Biomedical Engineering,  
Institute for Computational Engineering and Sciences,  
Department of Biomedical Engineering,  
Center for Cardiovascular Simulation,  
The University of Texas at Austin,  
Austin, TX 78712-1229  
e-mail: msacks@ices.utexas.edu

*Simulation of the mechanical behavior of soft tissues is critical for many physiological and medical device applications. Accurate mechanical test data is crucial for both obtaining the form and robust parameter determination of the constitutive model. For incompressible soft tissues that are either membranes or thin sections, planar biaxial mechanical testing configurations can provide much information about the anisotropic stress-strain behavior. However, the analysis of soft biological tissue planar biaxial mechanical test data can be complicated by in-plane shear, tissue heterogeneities, and inelastic changes in specimen geometry that commonly occur during testing. These inelastic effects, without appropriate corrections, alter the stress-traction*

*mapping and violates equilibrium so that the stress tensor is incorrectly determined. To overcome these problems, we presented an analytical method to determine the Cauchy stress tensor from the experimentally derived tractions for tethered testing configurations. We accounted for the measured testing geometry and compensate for run-time inelastic effects by enforcing equilibrium using small rigid body rotations. To evaluate the effectiveness of our method, we simulated complete planar biaxial test configurations that incorporated actual device mechanisms, specimen geometry, and heterogeneous tissue fibrous structure using a finite element (FE) model. We determined that our method corrected the errors in the equilibrium of momentum and correctly estimated the Cauchy stress tensor. We also noted that since stress is applied primarily over a subregion bounded by the tethers, an adjustment to the effective specimen dimensions is required to correct the magnitude of the stresses. Simulations of various tether placements demonstrated that typical tether placements used in the current experimental setups will produce accurate stress tensor estimates. Overall, our method provides an improved and relatively straightforward method of calculating the resulting stresses for planar biaxial experiments for tethered configurations, which is especially useful for specimens that undergo large shear and exhibit substantial inelastic effects. [DOI: 10.1115/1.4029266]*

**Keywords:** soft tissue mechanics, biaxial mechanical data, constitutive model

## 1 Introduction

A central need in the application of continuum mechanics to biological tissues is the development of the constitutive models. Such models are critical for insights into the development of accurate computational simulations of the heart and its valves, arteries, cartilaginous structures, and engineered tissue equivalents. While the formulation of the theoretical framework is always the first step, rigorous experimentation must be performed in parallel to explore all relevant deformations to both obtain the necessary constitutive model parameters and evaluate its predictive capabilities [1]. Thus, there is an increasing need for multi-axial mechanical data to fully explore and understand the complex structures of biological tissues. For incompressible planar membrane or thin soft tissue sections, a planar biaxial mechanical testing configuration can provide much information about the stress-strain behavior [1]. Planar biaxial tests can be performed with either extensional deformations only, or in combination with in-plane shear [2].

However, an ongoing problem in soft tissue mechanics is that they are not truly elastic. Soft tissues have been shown to exhibit elastic behavior under physiological conditions, yet also exhibit permanent setlike changes in configuration from preconditioning [1,3]. In addition, due to their very low stiffness in the zero stress state, even mounting and handling can alter the shape of the test specimen. This may result in a drastic change in the stress-free reference state of the specimen from the one measured prior to mounting. The situation becomes more complex when shear strains are involved. In our first studies [4], a simplified method was used to determine the components of the first Piola-Kirchhoff stress tensor  $\mathbf{P}$  from the initial dimensions and experimentally measured axial forces, with the second Piola-Kirchhoff stress tensor  $\mathbf{S}$  determined using  $\mathbf{S} = \mathbf{F}^{-1}\mathbf{P}$ . We later noted that this mapping did not produce fully accurate results in cases where the shear strain was substantial. An initial alternative method was developed [5], but was not a generalized solution. Specifically, the method did not account for changes in geometry of the unloaded state as a result of preconditioning and other related inelastic dimensional effects. As a result, the run-time specimen configuration will be a quadrilateral due to both shear and extensional strains that occurred during preconditioning. While others have developed various methods of deriving the stress under biaxial testing (e.g. Ref. [6]), no method to date addresses the actual

<sup>1</sup>Present address: School of Mechanical and Electronic Engineering, Soochow University, Suzhou, Jiangsu 512000, China.

<sup>2</sup>Corresponding author.

Manuscript received November 10, 2013; final manuscript received November 9, 2014; published online April 15, 2015. Assoc. Editor: Stephen M. Klisch.

testing geometry or compensates for changes in specimen geometry during the experiment. Moreover, inherent heterogeneities in tissue structure will always affect the accuracy of the resultant stress analysis. No systematic study to date has incorporated these effects nor determined their influence on the accuracy of stress tensor components from planar biaxial tests.

In approaching a solution to this problem, we first recognized certain key considerations and limitations inherent in interpreting any biaxial mechanical data. As noted in Sun et al. [7], no biaxial experimental configuration can produce an ideal homogeneous strain and stress state. This will result in subsequent errors in the computation of stress tensor components, which will propagate into the estimates of the material parameters, ultimately limiting our ability to accurately simulate soft tissues. Moreover, we believe one should first determine the constitutive model form and material parameters before undertaking the complex task of simulating complete organ systems. Thus, there remains a need for an improved method to derive the stress-strain relation directly from biaxial mechanical test data, with the assumption of homogeneous strain and stress fields.

The current work presents a straightforward, generalized approach for computing the effective Cauchy stress tensor for planar biaxial mechanical experiments that utilize a tethered mounting configuration. This method utilizes only the (1) the initial specimen dimensions, (2) the measured fiducial markers positions, and (3) the measured axial forces. It works under the assumption of homogeneous strain and stress fields within the specimen and compensates for the following attributes:

- (1) changes from the unloaded, initially measured specimen geometry to the postmounted, preconditioning state
- (2) the effects of structural heterogeneities in tissues, which can result in rigid body rotations
- (3) actual specimen geometry and tether attachment configurations during run time

To assist with validation and provide additional insights, we also present a comprehensive simulation of the entire biaxial testing geometry using simulated tissue properties, anisotropy, and structural heterogeneities.

## 2 Methods

**2.1 Kinematics of a Planar Biaxial Test.** Assuming a homogeneous deformation, the kinematical description of the planar biaxial test is

$$x_1 = \lambda_1 X_1 + \gamma_1 X_2, \quad x_2 = \lambda_2 X_2 + \gamma_2 X_1, \quad x_3 = \lambda_3 X_3 \quad (1)$$

where  $X_k$  and  $x_k$  are coordinates for material particles in the reference and current configurations, respectively,  $\lambda_k$  are the stretches and  $\gamma_k$  are the shears. The shear relative to the third axis is 0, with resulting deformation gradient tensor  $\mathbf{F}$

$$\mathbf{F} = \begin{bmatrix} \frac{\partial x_1}{\partial X_1} & \frac{\partial x_1}{\partial X_2} & \frac{\partial x_1}{\partial X_3} \\ \frac{\partial x_2}{\partial X_1} & \frac{\partial x_2}{\partial X_2} & \frac{\partial x_2}{\partial X_3} \\ \frac{\partial x_3}{\partial X_1} & \frac{\partial x_3}{\partial X_2} & \frac{\partial x_3}{\partial X_3} \end{bmatrix} = \begin{bmatrix} \lambda_1 & \gamma_1 & 0 \\ \gamma_2 & \lambda_2 & 0 \\ 0 & 0 & (\lambda_1 \lambda_2 - \gamma_1 \gamma_2)^{-1} \end{bmatrix} \quad (2)$$

Note that  $\mathbf{F}_{33} = \lambda_3 = (\lambda_1 \lambda_2 - \gamma_1 \gamma_2)^{-1}$  is computed by the incompressibility constraint  $\det(\mathbf{F}) = 1$ . All specimen deformations are assumed to be completely quantified from the interior of the specimen (approximately the inner third by linear dimension or area) using fiducial markers or texture mapping techniques [1,8].

## 2.2 Analysis of Stress

### 2.2.1 Planar Biaxial Testing Experimental Configuration.

Planar biaxial devices follow a typical design overall, but vary in the specific boundary conditions utilized. We start with a rectangular specimen with known side lengths  $L_1$  and  $L_2$ , and an initial thickness  $L_3$ , and then mounted with resultant forces  $\mathbf{f}^{(1)}$  and  $\mathbf{f}^{(2)}$  (Fig. 1). Previously, we determined the stresses using

$$P_{11} = \frac{f_1^{(1)}}{A^{(1)}}, \quad P_{22} = \frac{f_2^{(2)}}{A^{(2)}}, \quad P_{12} = P_{21} = 0, \quad \mathbf{P} = \begin{bmatrix} P_{11} & P_{12} \\ P_{21} & P_{22} \end{bmatrix} \quad (3)$$

where  $\mathbf{f}^{(i)}$  and  $A^{(i)}$  are the axial forces and initial cross-sectional areas, respectively, with  $i = 1, 2$  [4]. The Cauchy stress  $\mathbf{t}$  and

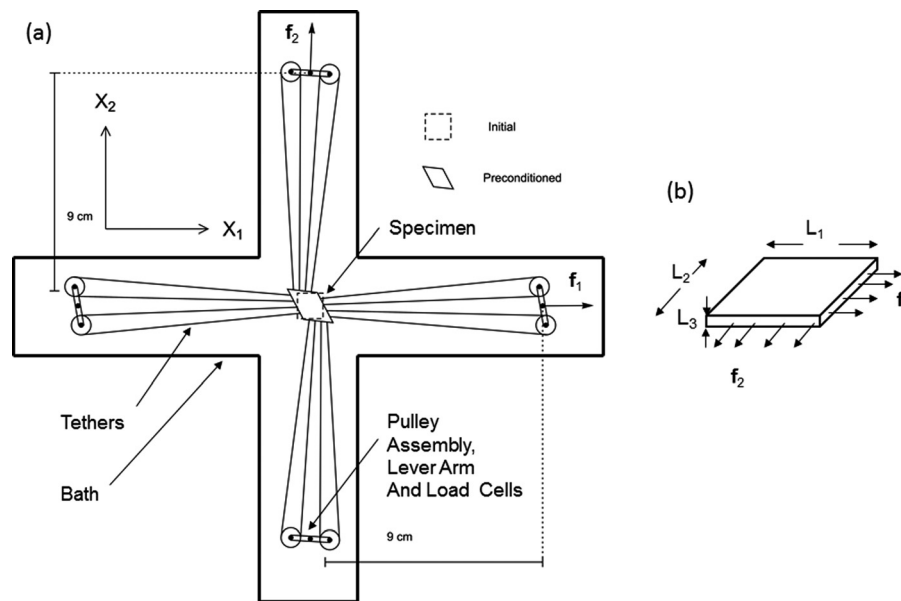


**Fig. 1 (a) Typical biaxial mechanical test configuration and (b) schematic of the forces and dimensions. Note that  $\mathbf{f}^{(1)}$  acts on an area of  $A^{(1)} = L_2 \times L_3$  and  $\mathbf{f}^{(2)}$  on  $A^{(2)} = L_1 \times L_3$ .**

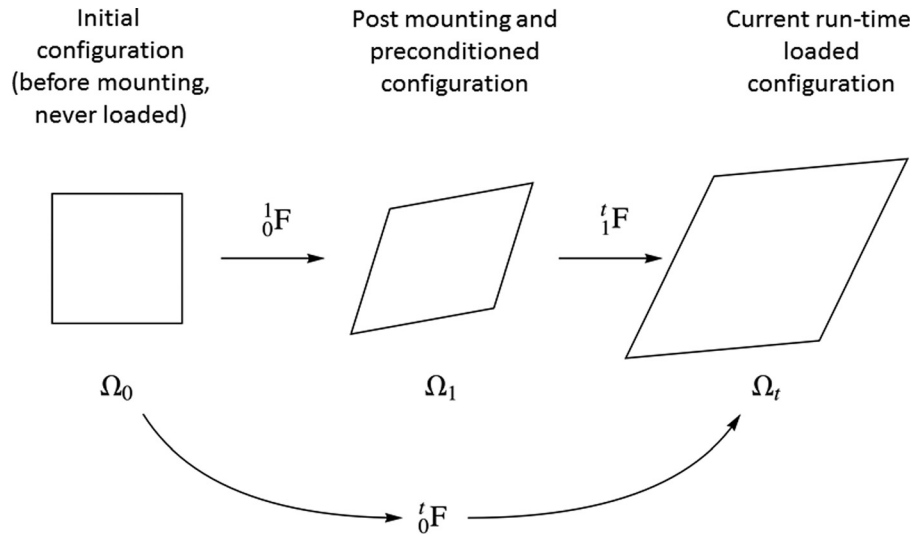


**Fig. 2** Different specimen configurations used during biax testing.  $\Omega_0$  is the original stress-free and undeformed free floating state.  $\Omega_1$  is an intermediate configuration due to mounting, preconditioning and other inelastic run-time effects, which can be described by the deformation  ${}^1_0\mathbf{F}$ .  $\Omega_t$  is the current deformed state. The overall change in configuration is given by  ${}^t_0\mathbf{F}$ , where the deformation due to stress is given by  ${}^t_1\mathbf{F}$ .

second Piola–Kirchhoff stress tensor  $\mathbf{S}$  are computed using standard formulations  $\mathbf{t} = \mathbf{P} \cdot \mathbf{F}^T$  and  $\mathbf{S} = \mathbf{F}^{-1}\mathbf{P}$ .

It should be noted that the methods of attachment are generally separated into tethered [1,9–12] and clamped boundaries [13–17]. In the present work, we focus on tethered boundary configurations. We do not intend to convey that any particular method is optimal for any application, but rather to show that a tethered attachment system, with its ability to allow free lateral displacements and to apply relatively uniform distribution of boundary forces, can be used to accurately obtain the stress–strain relation directly from the experimentally obtained data. We feel this is important as the first step in any tissue mechanical analysis in order to establish the form of the strain energy function, which is best done using directly determined  $\mathbf{S}$  and  $\mathbf{F}$  whenever possible. As such, this method will only require direct measurement of (1) initial specimen dimensions, (2) fiducial marker positions, and (3) the measured axial forces. Due to the intrinsic differences in the stress state induced, this method will not be directly applicable to clamped boundaries. Additionally, the following assumptions are made throughout the present work:

- (1) The tissue is at all times in quasi-static equilibrium.
- (2) The deformations are homogeneous, and consequently:
  - (a) The specimen is located at the center of the apparatus and does not translate.
  - (b) The testing system is symmetric.
- (3) The applied tractions are evenly distributed per side, given by the average applied by the four attached tethers.

**2.2.2 Mounting and Preconditioning Effects.** Distortions will occur to some extent during mounting and testing due to the high compliance of soft tissue specimen in the low stress range. Although the mechanisms for preconditioning effects remain unknown, it is known that the effect is not strictly viscoelastic [1,18,19]. Instead, it is similar to permanent-setlike effects, but is reversible over time [1]. For example, it has been shown that the process itself reverts over the course of 24 h in chemically treated pericardium tissue [1]. Thus, the effect only lasts for the current test and is utilized to induce a stable, repeatable response [1,18,19]. The new unloaded configuration can be quite different from the initial rectangular state.

To compensate for these effects, we first establish the following configurations (Fig. 2). The initial free floating state  $\Omega_0$  is defined to be the initial state of the specimen immediately after being cut to size, and is well defined and rectangular. After mounting, preconditioning, and other inelastic run-time effects, the specimen is then fully unloaded and the new unloaded geometry is defined as  $\Omega_1$ . We define a deformation  ${}^1_0\mathbf{F}$  which maps  $\Omega_0$  to  $\Omega_1$ .  $\Omega_1$  is the reference configuration used for all stress and strain calculations, with the associated deformation  ${}^t_0\mathbf{F}$ .

Direct dimensional measurements of  $\Omega_1$  requires removing the specimen from the device, which must be done carefully to avoid damaging the tissue and inducing additional distortions. An alternative is to image the specimen in situ, which poses its own sets of challenges. Moreover, stress is only induced in the region bounded by the tethers [13,16,17], with the surrounding tissue deforming minimally. Therefore, the tether bounded area is best used for the specimen geometry. As a result, the preconditioning effects are accrued in the region of interest (ROI, region bounded by the markers) may not be represented by the visible edges of the specimen. However,  $\Omega_1$  can be easily estimated from the deformation in the inner region of the specimen via the fiducial markers, assuming the overall specimen deformation is approximately homogeneous. This simplifies the approach and also provides an easy way of determining the thickness, all without physically removing the specimen from the device. We will thus assume that  $\Omega_0$  is known precisely and that the specimen undergoes a homogeneous deformation quantified by the strain measurement. Note that the magnitude of preconditioning effects can vary considerably in different tissues. For example, it can be modest for a heart valve leaflet (Fig. 3(a)) or very significant for a murine right ventricle (RV) free wall tissue specimen (Fig. 3(b)).

**2.2.3 Equilibrium.** In direct analysis of biaxial experimental data, we have observed that the shear components of  $\mathbf{t}$  derived from the previous methods [5] will not be equal, violating equilibrium. In addition to preconditioning and inelastic effects, the overall geometry and orientation of the specimen are not exactly predicted by the deformation at the center region of the specimen due to real tissue heterogeneities. These will induce the specimen to rotate slightly (i.e., undergo rigid body rotation) with respect to the applied forces, leading to no net moment on the specimen as a whole. This difference between the rigid body angle

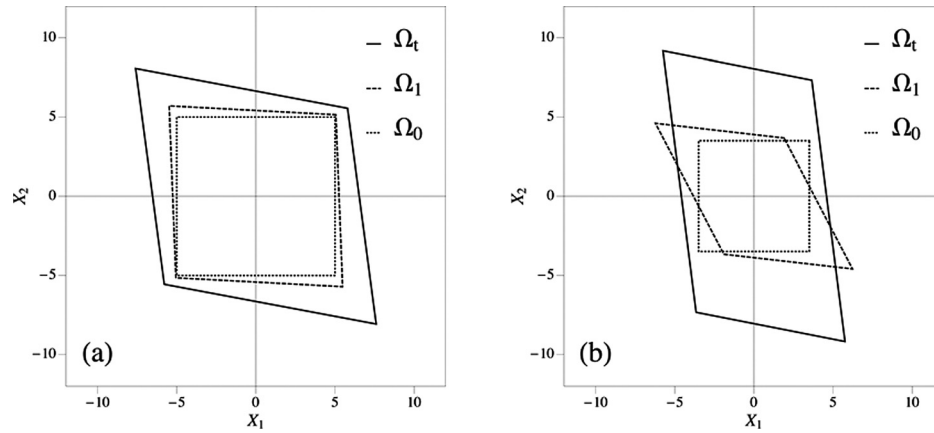


**Fig. 3** The configurations  $\Omega_0$ ,  $\Omega_1$ , and  $\Omega_t$  for a glutaraldehyde treated aortic valve leaflet (a) and the RV myocardium (b) are shown. These represent the typical change in the reference configuration for a typical biaxial experiment due to preconditioning and other inelastic run-time effects. Note that the RV data, tissue is sheared in the negative direction during preconditioning. It is then sheared back in the positive direction during loading.

calculated with respect to the center of the specimen and the real rigid body angle produces a small angular moment in the derived stress.

To account for this, we assume the body forces are negligible, and the rigid body moment  $\mathbf{M}$  is given by

$$\mathbf{M} = \int_S \mathbf{r} \times \mathbf{T} dS \quad (4)$$

where  $\mathbf{r}$  is the position vector and  $\mathbf{T}$  is the boundary traction vector (Appendix). We parameterize  $\mathbf{r}$  as  $\mathbf{r}(s, \theta) = s \mathbf{x}^2 + (1-s) \mathbf{x}^1$ ,  $s \in [0, 1]$ , where  $\mathbf{x}^1 = {}^t_0\mathbf{F}(\theta) \cdot \mathbf{X}^1$  and  $\mathbf{x}^2 = {}^t_0\mathbf{F}(\theta) \cdot \mathbf{X}^2$  are the corner points bounding the sides in the current state,  $\theta$  is the rigid body angle of the deformation gradient, and  $l_3$  is the current thickness. Thus, we are left with the sum of the following integral for all four sides:

$$M_3(\theta) = l_3 \int_0^1 (\mathbf{r}(\theta, s) \times \mathbf{T}) |\mathbf{r}'(\theta, s)| ds \quad (5)$$

We note that in the present system (Fig. 1(a)) the orientation of the traction  $\mathbf{T}$  changes as the specimen deforms, and we thus employ the following approach to enforce momentum balance by adjusting  $\theta$  (Fig. 4). The initial estimate of the rigid body angle,  $\theta$ , is derived from the deformation gradient  ${}^t_0\mathbf{F}$ . Based on  $\theta$ , the quantities describing the current geometry (e.g., tether orientations, the Appendix) are derived. The first moment can be calculated according to Eq. (5) and can serve as a tolerance check. If the moment does not converge to zero, a new rigid body angle  $\theta$  is proposed and the process is repeated until equilibrium is satisfied. Once the best  $\theta$  is found, the current geometry of the specimen can be determined from the deformation gradient  ${}^t_0\mathbf{F}$ . This, when paired with the known tractions  $\mathbf{T}$ , allows us to determine the

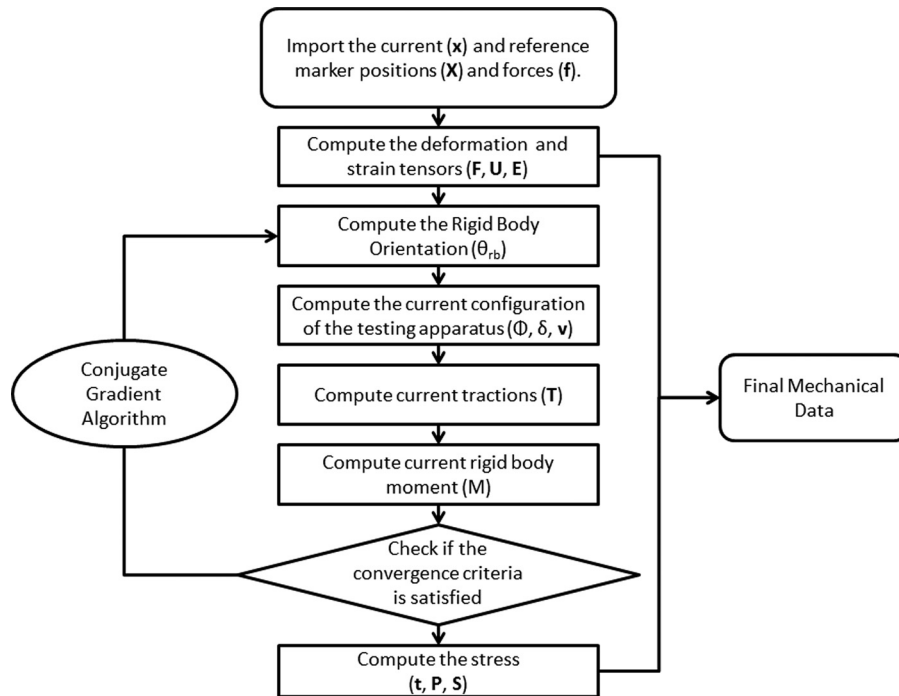


**Fig. 4** Flowchart of for the geometric rigid body moment minimization and the simulation of the biaxial geometry and stresses



Cauchy stress from  $\mathbf{T} = \mathbf{t} \cdot \mathbf{n}$ . In practice, the rigid body rotation is well within the experimentally measured rigid body rotations, typically  $< 3$  deg. Note that all calculations were implemented in a custom written Mathematica 10 program.

**2.2.4 Final Stress Analysis.** As stated above, we assume that the initial specimen geometry is known and that the specimen undergoes a homogenous deformation quantified by the interior strain measurements. We can thus calculate the current geometry using the deformation gradient. Let  $d\mathbf{l}$  be a vector representing the side of the tissue in the current configuration and  $d\mathbf{L}$  representing the side of the tissue in the initial free floating configuration, then we can calculate the current side lengths and thickness ( $l_1, l_2, l_3$ ) according to

$$d\mathbf{l} = \mathbf{F} \cdot d\mathbf{L}, \quad l = \sqrt{d\mathbf{l} \cdot d\mathbf{l}}, \quad l_3 = \lambda_3 L_3 a \quad (6)$$

where  $L$  is the initially measured side lengths. The current surface area are  $a^{(1)} = l_2 l_3$  and  $a^{(2)} = l_1 l_3$ . The outward surface normal,  $\mathbf{n}$ , can be calculated by taking the cross product of the line parallel to the surface and a unit vector pointing along  $X_3$

$$\mathbf{n} = \frac{d\mathbf{l} \times \mathbf{e}_3}{|d\mathbf{l} \times \mathbf{e}_3|} \quad (7)$$

The total axial force for each side is  $\mathbf{f} = f_1 \mathbf{e}_1 + f_2 \mathbf{e}_2$ , where  $f_1$  is the component along the  $X_1$  axis and  $f_2$  is the component along the  $X_2$  axis. Often the axial forces are assumed to be aligned to the experimental axes. This is not true under shear and can produce significant differences and even reverse the sign of the shear stress. In the case when the load cells are unidirectional, only the forces along the axes  $f_1^{(1)}$  and  $f_2^{(2)}$  are measured. Given the direction of the traction (Appendix),  $\mathbf{v}$ , the off axis forces can be obtained by multiplying the on-axis force by the ratio of its components, i.e.,  $f_2 = f_1 v_2^{\text{avg}} / v_1^{\text{avg}}$ . The net traction vector  $\mathbf{T}$  is thus

$$\begin{aligned} \mathbf{T}^{(1)} = -\mathbf{T}^{(3)} &= \left[ \frac{f_1^{(1)}}{a^{(1)}}, \frac{f_1^{(1)} v_2^{\text{avg},(1)}}{a^{(1)} v_1^{\text{avg},(1)}} \right], \\ \mathbf{T}^{(2)} = -\mathbf{T}^{(4)} &= \left[ \frac{f_2^{(2)} v_1^{\text{avg},(2)}}{a^{(2)} v_2^{\text{avg},(2)}}, \frac{f_2^{(2)}}{a^{(2)}} \right] \end{aligned} \quad (8)$$

We can now re-express Cauchy's theorem,  $\mathbf{T} = \mathbf{t} \cdot \mathbf{n}$ , using the normal and traction vectors from all four sides as

$$\begin{bmatrix} n_1^{(1)} & n_2^{(1)} & 0 \\ 0 & n_1^{(1)} & n_2^{(1)} \\ n_1^{(2)} & n_2^{(2)} & 0 \\ 0 & n_1^{(2)} & n_2^{(2)} \end{bmatrix} \cdot \begin{bmatrix} t_{11} \\ t_{12} \\ t_{22} \end{bmatrix} = \begin{bmatrix} T_1^{(1)} \\ T_2^{(1)} \\ T_2^{(2)} \\ T_1^{(2)} \end{bmatrix}, \quad \mathbf{t} = \begin{bmatrix} t_{11} & t_{12} \\ t_{12} & t_{22} \end{bmatrix} \quad (9)$$

This allows us to solve for the Cauchy stress tensor  $\mathbf{t}$  using least square regression. Based on incompressibility  $J = \det(\mathbf{F}) = 1$ , the first and second Piola-Kirchhoff stress tensors,  $\mathbf{P}$  and  $\mathbf{S}$ , can be determined from  $\mathbf{t}$  as

$$\mathbf{P} = \mathbf{t} \cdot \mathbf{F}^{-T}, \quad \mathbf{S} = \mathbf{F}^{-1} \cdot \mathbf{t} \cdot \mathbf{F}^{-T} \quad (10)$$

### 2.3 FE Simulations of the Biaxial Test and Specimen Heterogeneity

**2.3.1 Structural Model.** An incompressible structural model [1,20–23] under the framework of hyperelasticity was used for FE simulation to describe the underlying mechanisms of soft biological tissues, with the commercial FE simulation software ABAQUS (6.12, Simulia, RI). The full structural model corresponding to Eq. (12) in Fan and Sacks [20] was used, with the parameters listed in Table 2 as follows:  $\phi_f$  (volume fraction of fibers),  $\eta_f$  (fiber elastic modulus),  $V_m$  (volume fraction of matrix), and  $\mu_m$  (elastic modulus of the matrix),  $\mu$  (mean direction of the fiber splay), and  $\sigma$  (standard deviation of the fiber splay).

**2.3.2 Biaxial Test Simulations.** To simulate an experimentally realistic biaxial test, tether lines and pulleys were included in the FE model. Initial position of each pulley and tether line prior to applying biaxial forces was calculated using the proposed analytical method (Figs. 5(b) and 5(c)). The pulley was simplified by a steel bar with a circular cross section. The bar was connected to the tether lines and connection bars (Fig. 5(a)). The bars were set to planar motion in the  $x_1$ - $x_2$  plane. The center of the bar was constraint to linear movements along the corresponding  $X_1$  or  $X_2$  axis. No other constraints were applied to the model; all other elements were allowed to move freely within the framework. ABAQUS element B31H was used for meshing both the tether lines and pulley

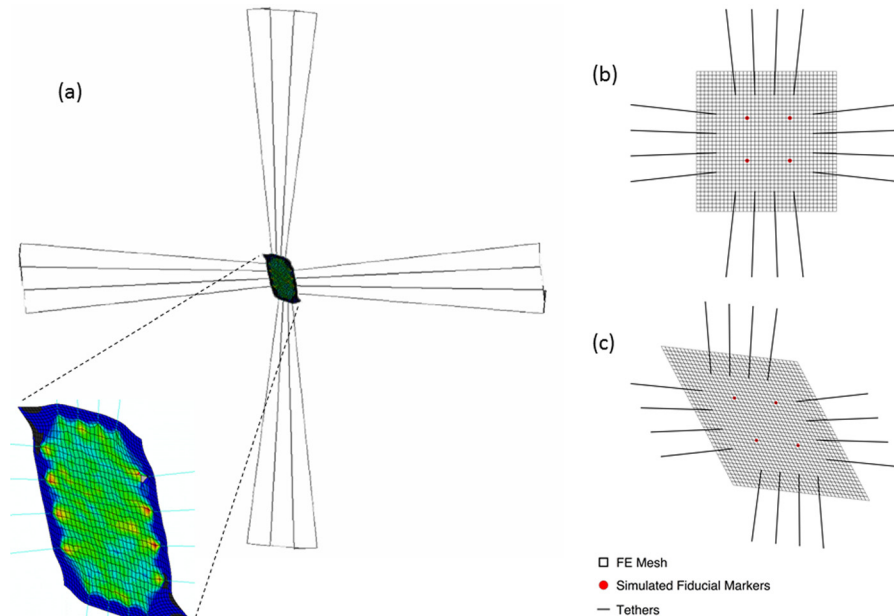


**Fig. 5.** (a) The main components of the biaxial system are constructed and simulated in FE. The (b) free floating and (c) preconditioned states are shown.

**Table 1 Geometric parameters of a sample**

Sample size (mm <sup>2</sup> )	Thickness (mm)	Element number	Element size (mm <sup>2</sup> )	ROI (marker) size (mm <sup>2</sup> )
7 × 7	0.768	35 × 35	0.2 × 0.2	2.2 × 2.2

bars. The size of a typical initial free floating sample was used. The sample was meshed by 1225 ABAQUS M3D4 type elements (Figs. 5(b) and 5(c)). Detailed sample geometry is shown in Table 1. The preconditioned geometry was acquired by applying a deformation gradient to the square shaped sample. The deformation gradient was experimentally acquired from an ovine RV wall sample. The structural model was used for sample material. Standard steel material was used for the tether lines and pulley bars. All material parameters used are summarized in Table 2.

To evaluate the analytical method, samples with four different fiber distributions were considered in this study. The fiber distribution parameters were chosen in a similar way as presented by Lee et al. [24]. The mean value of preferred fiber direction ( $\mu$ ) was chosen to be either 0 or 45 deg with respect to the  $X_1$  axis. The mean value of fiber splay ( $\sigma$ ) was chosen as 15 and 30 deg, to represent typical cases of the aortic valve [25,26] and pericardium [27], respectively. The standard deviation of the fiber preferred direction and splay was chosen as 15 and 5 deg (Table 3). An illustration of fiber distribution for both square shaped and preconditioned samples is shown in Fig. 6.

Four different tether placement configurations for biaxial testing were constructed to investigate the effects of tether placement. To test the maximum coverage of the effective region of the sample, an ideal case with tether attachment points placed with a gap of 9 mm at the edge of the sample was constructed (A) (Fig. 7(a)). To test for slight misplacement of the tethers in practical experiments, another sample with the same tether attachment gap but with a 0.6 mm offset to the edge of the sample was also constructed (B) (Fig. 8(a)). To test the effect of a narrowly placed tether attachment points, a case with attachment gap of 5 mm placed at the edge of the sample (C) (Fig. 9(a)). Finally, an experimentally realistic case with tether points 1 mm offset to the sample edge (D) (Fig. 10(a)) were also simulated (closest to the experimental case). For samples with fiber splay of 15 deg, equibiaxial forces up to 420 mN were applied to the center point of each side of the pulley bars; for samples with fiber splay of 30 deg, equibiaxial forces up to 840 mN were applied. The positions of the four markers were exported at each force increment step for analysis using both the previous and new methods. Mean Cauchy stress within the ROI was calculated and compared with results from analytical methods.

**2.3.3 Methods Comparison.** The FE simulation results provided detailed stresses at the element level, thus the results from the other two analytical methods were compared with the results of FE simulation to evaluate the goodness of the estimation. A normalized root mean square error (NRMSE) with respect to the

maximum value was used to quantify the performance of the two analytical methods, with

$$\text{NRMSE} = \frac{1}{|t_{\max}^a - t_{\min}^a|} \left( \frac{1}{n} \sum_n (t_i^a - t_i^{\text{FE}})^2 \right)^{1/2} \quad (11)$$

where  $t^a$  is the Cauchy stress from the analytical methods,  $t^{\text{FE}}$  is the Cauchy stress from the FE simulation, and  $n$  is the number of total force increment steps.

### 3 Results

**3.1 Effects of Tether Placement.** The distribution of Cauchy stress tensor components  $t_{11}$  and  $t_{22}$  of four tether configurations from both square shaped sample and preconditioned sample (Figs. 7–10) shows the effects of different tether placements. In both cases, the samples with preferred fiber directions all along the  $X_1$  axis with fiber splay of 15 deg were chosen for illustration. The sample with relatively closely placed tether attachment points (Fig. 8(b)) has a relatively more heterogeneous stress distribution, and the corresponding stress magnitude is lower. In analyzing square shaped samples, both the old and new methods provide the best estimate in configurations (A) and (D), while the estimate of stress has a relatively large error in configuration (C), as illustrated for the material model I (Fig. 9). A summary of NRMSE of both methods for square shaped sample is shown in Table 4. Configuration (A) has the least mean NRMSE in estimating  $t_{11}$  while (D) has the least mean NRMSE in estimating  $t_{22}$ . The mean NRMSE of both configurations (A) and (D) is within 5%.

**3.2 Analyzing Biaxial Test Data From a Preconditioned Specimen.** When the preconditioned configuration was used, the shear component of the Cauchy stress became substantial (Fig. 8). The NRMSE of tensile stresses estimation of the old method is larger than the new method for all tether configuration cases (Table 4). In comparison, the new method provides a better estimate of both tensile and shears stress components. In tether configuration (D), the estimate of shear stress components is the best with a mean NRMSE of 3.6%. Configuration (B) provides the best estimate of  $t_{11}$  component while configuration (A) provides the best estimate of  $t_{22}$ . The mean NRMSEs for both configurations (A) and (D) are within 10% for all stress components.

**3.3 Key Results.** For ideal cases, without shear, heterogeneities and preconditioning effects, both the previous and current methods preform optimally with no errors as expected. When

**Table 2 Material parameters of the sample, tether line, and pulley bar**

Structural material of the sample						
$\alpha$	$\beta$	$\eta_f$ (MPa)	$\varepsilon_{ub}$	$d_c$	$\phi_c$	$\mu_m$ (MPa)
6.43	1.5	100	0.8	1	0.3	0.02
Tether lines and pulley bars						
$E$ (GPa)	$\nu$					
200	0.3					

**Table 3 Parameters of fiber distribution for tested samples.  $\mu_{PD}$  is the mean value of the preferred fiber direction,  $\sigma_{PD}$  is the standard deviation of the preferred fiber direction,  $\mu_\sigma$  is the mean value of the preferred fiber direction standard deviation,  $\sigma_\sigma$  is the standard deviation of the preferred fiber direction standard deviation.**

Fiber distribution	$\mu_{PD}$ (deg)	$\sigma_{PD}$ (deg)	$\mu_\sigma$ (deg)	$\sigma_\sigma$ (deg)
Material model I	0	15	15	5
Material model II	45	15	15	5
Material model III	0	15	30	5
Material model IV	45	15	30	5

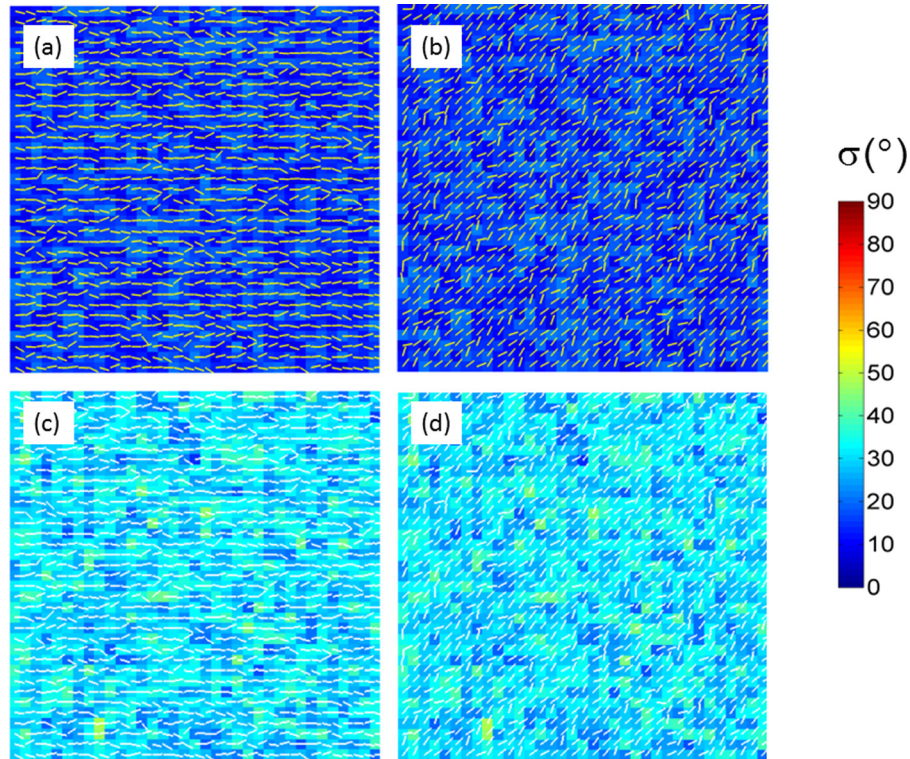


Fig. 6 The four material models used in the heterogeneous specimens. They are for pericardium tissue (a) and (b) and valvular tissues (c) and (d). The specimen is rotated for normal loading (a) and (c) and shear loading (b) and (d).

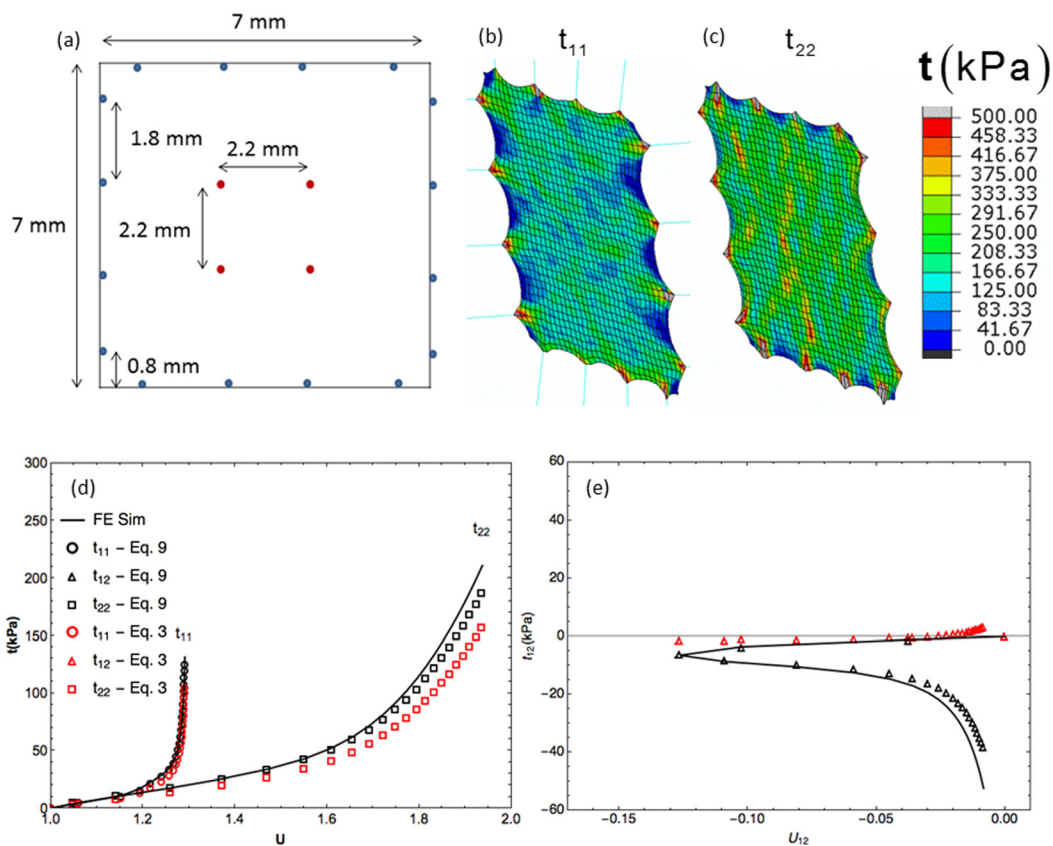


Fig. 7 The results for the preconditioned pericardium specimen with (a) tether arrangement (A). The (b)  $t_{22}$  stress distribution, (c) normal stresses, and (d) shear stresses are shown.



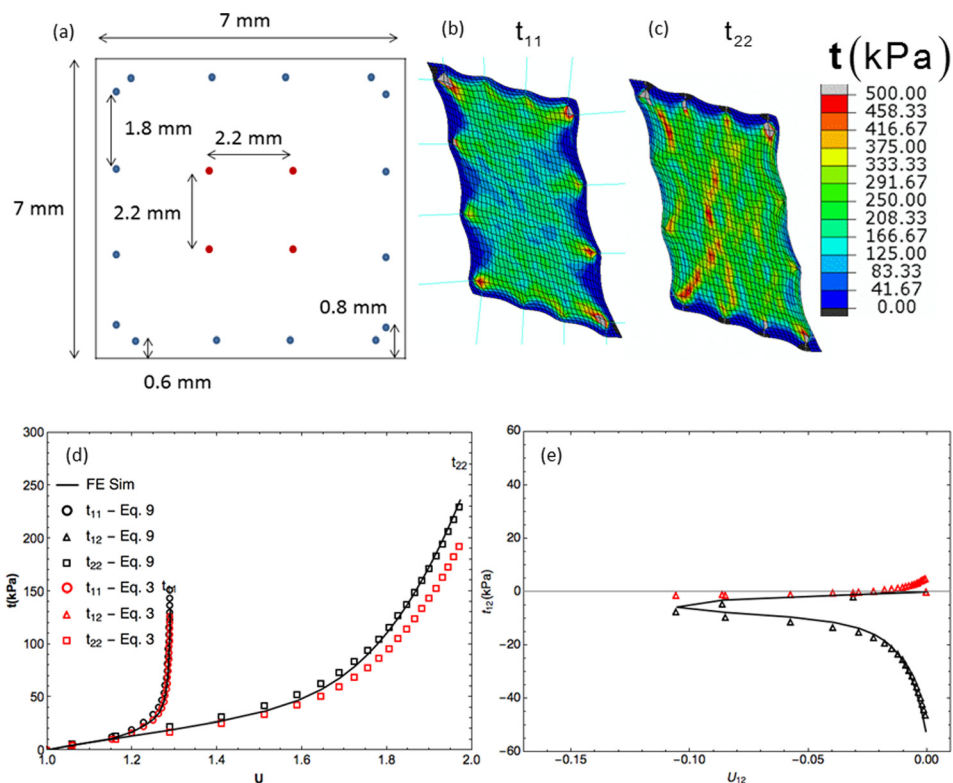


Fig. 8 The results for the preconditioned pericardium specimen with (a) tether arrangement (B). The (b)  $t_{22}$  stress distribution, (c) normal stresses, and (d) shear stresses are shown.

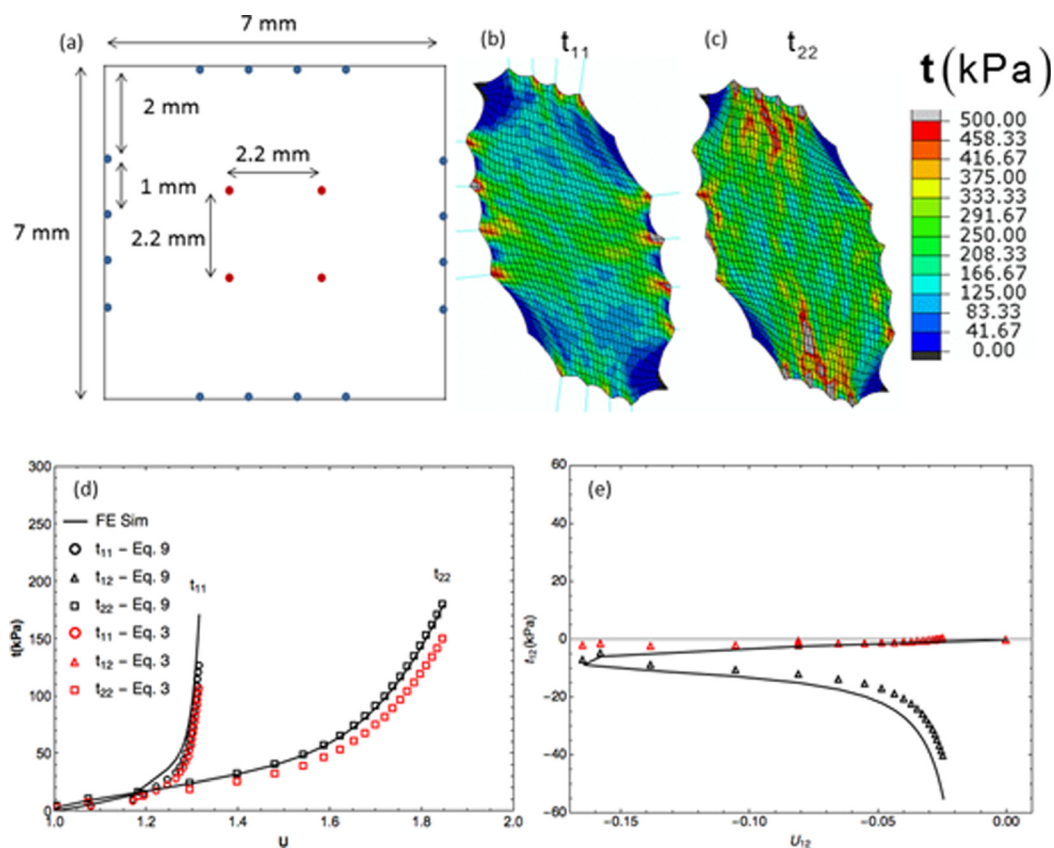


Fig. 9 The results for the preconditioned pericardium specimen with (a) tether arrangement (C). The (b)  $t_{22}$  stress distribution, (c) normal stresses, and (d) shear stresses are shown.



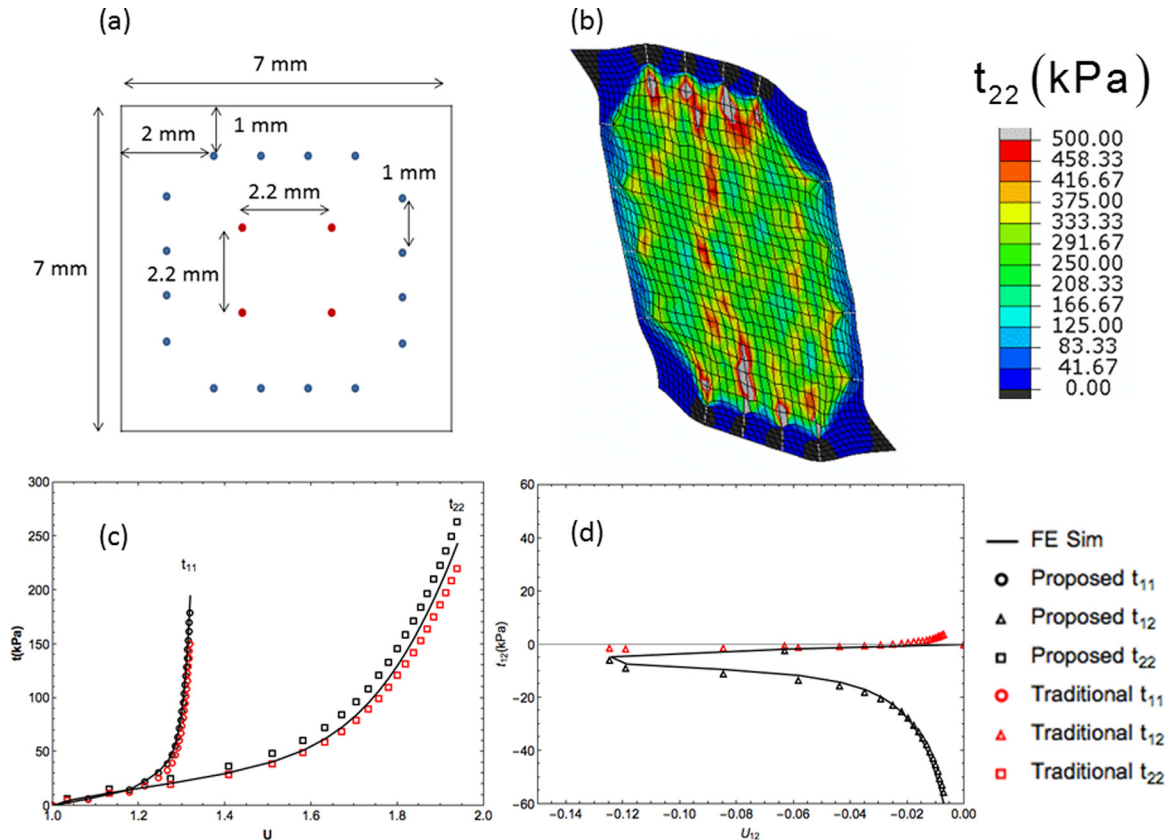


Fig. 10 The results for the preconditioned pericardium specimen with (a) tether arrangement (D). The (b)  $t_{22}$  stress distribution, (c) normal stresses, and (d) shear stresses are shown.

Table 4 NRMSE of the estimated Cauchy stress components for both square shaped and preconditioned pericardial specimens using both new and old methods. The tether placement used is shown (Fig. 5).

NRMSE	Tethered configuration	$t_{11}$	$t_{22}$	$t_{12}$	$t_{11}$	$t_{22}$	$t_{12}$
		Eq. (9)			Eq. (3)		
square	(A)	$0.94 \pm 0.51\%$	$4.40 \pm 3.88\%$	—	$0.94 \pm 0.52\%$	$4.34 \pm 3.89\%$	—
	(B)	$6.26 \pm 1.58\%$	$3.89 \pm 2.16\%$	—	$6.27 \pm 1.59\%$	$3.90 \pm 2.18\%$	—
	(C)	$13.75 \pm 7.62\%$	$9.98 \pm 11.13\%$	—	$13.87 \pm 7.80\%$	$9.74 \pm 10.74\%$	—
	(D)	$2.92 \pm 2.20\%$	$3.31 \pm 2.46\%$	—	$2.97 \pm 2.28\%$	$3.21 \pm 2.32\%$	—
preconditioned	(A)	$6.27 \pm 3.65\%$	$3.67 \pm 1.69\%$	$6.33 \pm 8.33\%$	$17.39 \pm 5.79\%$	$13.39 \pm 3.74\%$	$1116.52 \pm 1632.75\%$
	(B)	$4.18 \pm 1.47\%$	$5.85 \pm 3.30\%$	$10.59 \pm 4.52\%$	$4.88 \pm 2.02\%$	$7.40 \pm 2.80\%$	$905.05 \pm 1372.93\%$
	(C)	$27.27 \pm 10.74\%$	$2.44 \pm 1.57\%$	$26.30 \pm 3.95\%$	$43.33 \pm 16.14\%$	$12.46 \pm 4.93\%$	$641.57 \pm 566.48\%$
	(D)	$8.54 \pm 4.01\%$	$6.67 \pm 1.60\%$	$3.60 \pm 1.91\%$	$20.35 \pm 6.47\%$	$6.50 \pm 11.81\%$	$609.92 \pm 678.60\%$

these effects are introduced, we found that the presented method offers a significant improvement in the estimates for the shear stress and minor improvements in the normal components (Table 4). The more significant effect, previously unaccounted for, was in regard to the tether placements. The region of the specimen lying outside of the tether bounded region was found to be under insignificant amount of stress, resulting in the stress of the ROI being higher than previously expected. Correcting the specimen dimensions based on the tether position also corrects the associated stress estimates. In the ideal tether layout (Fig. 7), we can obtain the most accurate stress estimates (Table 4). Minor differences in the tether positions and introducing a border to surround the tether (Fig. 10) produce only small error in the stress, while more significant deviations in the layout can produce larger errors (Table 4).

## 4 Discussion

**4.1 Accuracy of the Method.** Our aim was to devise a method to accurately obtain the stress-strain behaviors directly

from the measured data from planar biaxial tests. It is important for the method itself to be independent of the particulars of the specimen's mechanical properties and any constitutive model formulation, so that it may serve as a starting point for establishing the form of the strain energy function. We found that this is achieved using a system of tethers to apply forces with no restriction on the lateral displacement. As an extension to the previous simulation of biaxial experiments [13,16,17,28], we included the real tissue heterogeneities, anisotropy, and preconditioning, as well as the carriage and attachment geometries, to simulate as close to the real conditions of planar biaxial experimental configurations as possible.

The primary findings were that the main source of error is the shear induced due to tissue anisotropy and preconditioning, and heterogeneous deformations. These effects are most easily observed as a violation of equilibrium [5]. We found that our method corrects these effects and produces accurate estimates of the mean stresses within the ROI (Table 4), although its effect on accuracy depends on the specifics of the tissue used (Tables 4

**Table 5 NRMSE of the estimated Cauchy stress components for both square shaped and preconditioned valvular specimens using both new and old methods**

NRMSE	Tethered configuration	$t_{11}$	$t_{22}$	$t_{12}$	$t_{11}$	$t_{22}$	$t_{12}$
			Eq. (9)			Eq. (3)	
square	(A)	1.19%	4.84%		1.19%	4.84%	
	(B)	7.46%	1.16%		7.46%	1.16%	
	(C)	14.93%	5.56%		14.93%	5.56%	
	(D)	2.54%	6.96%		2.54%	6.96%	
preconditioned	(A)	1.98%	2.41%	1.69%	13.04%	12.47%	279.07%
	(B)	7.81%	3.23%	8.22%	1.7%	6.4%	239.79%
	(C)	17.87%	4.81%	6.09%	31.23%	4.48%	331.64%
	(D)	2.96%	7.78%	3.58%	13.85%	0.83%	232.32%

and 5). There was also some expected loss of accuracy in the preconditioned state due to the homogeneous assumption, where the true preconditioned state differs slightly from the affine mapping. However, the error produced is very small. It is also important to note that the previous method (Eq. (3)) does not produce significantly worse estimates of the true axial components of the stress (Figs. 7–10). This lends confidence in the results of the previous works. One major improvement of the previous method is in estimating the shear stress, where Eq. (9) can cause sign errors (Figs. 7(e)–10(e)).

**4.2 Preconditioning Effects.** Since the time of Fung [29], the soft tissue biomechanics community has adopted a pseudohyperelastic framework to describe tissue elasticity. However, the inelastic effects exhibited during experiments still need to be accounted for. The method described herein does not require a full understanding of these effects; only the initial dimensions, the fiducial marker positions, and the forces along each axis are needed. Any changes in the configuration can be accounted for by keeping track of the relevant reference states. Under no shear and negligible changes in the reference configuration due to preconditioning or other inelastic run-time effects, there is generally no need for the present corrections. However, small misalignments of the material axes of an anisotropic sample with the experimental axes will result in shear that can produce errors in the computed stress components necessitating the method described. Typically when there is shear there will be a net moment generated. Using the experimentally measured deformation gradient, the net moment is on the order of  $1 \text{ N} \cdot \text{mm}$ . This effect is small and can be accounted for by changing the rigid body angle by  $0 \text{ deg}$ – $5 \text{ deg}$ . For homogeneous rectangular specimens, where we expect the least difference between the deformation of the ROI and the whole specimen, this change in angle is negligible. For heterogeneous preconditioned specimens, where there should be the greatest difference between the ROI and the whole specimen, the change of the rigid body angle is up to  $0.81 \text{ deg}$ . We note that this has been seen to be high in real experimental results that are subjected to additional complications. While this change is typically small, it is necessary to compensate for the rotation induced by the heterogeneity of the tissue, which would otherwise be ignored in the reduction of data to enforce the assumption of homogeneity. It also ensures the correct stress to traction mapping and equilibrium ( $t_{12} = t_{21}$ ).

**4.3 Effect of Tethered Configuration.** Perhaps the most important factors that were not explored in the previous literature are the position of the tethers, heterogeneity in tissue structure, and the effective specimen geometry [13,16,17,28]. In the present work, we explored four different arrangements of tethers (Figs. 7–10) and found the region bounded by tethers to be the most reliable estimate for the effective specimen dimensions. This is the result of the forces being applied not to the edge of the specimen but rather to some inner region. Take for instance Fig. 4(e)

from Ref. [13] and Figs. 7(b), 7(c), 10(b), and 10(c) in the present work, in all cases nonzero stresses occur only in the region bounded by the tethers. This essentially results in an “effective specimen size” that is smaller than the actual dimensions of the specimen. This is purely a magnitude error, but can be quite significant. The ideal position to place the tethers is rather intuitive: Tethers should divide a side equally and this consistently produced the best results (Fig. 7).

**4.4 Effect of Material Model and Heterogeneities.** Any reliable method used to evaluate the mechanical properties, particularly biological tissues, should not depend on knowing the mechanical properties a priori. For this purpose, we chose two material models based on typical aortic valve [25,26] and pericardium [27] tissue (Table 4), and introduced heterogeneities based on Lee et al. [24] to evaluate the associated error and validity of the homogeneous assumption. We noticed no difference in our ability to estimate the stresses based on the material model, and the estimated stress is comparable to the mean stress of the ROI for the FE simulation (Figs. 7–10). Furthermore, the stresses,  $t_{11}$  and  $t_{22}$ , are equal up to machine precision when the rigid body minimization is done with sufficient accuracy as compared to the previous results [5]. Overall, this method is sufficient to compensate for any rigid body effect due to the heterogeneities in the central region and for the assumption of homogeneity to hold for typical valvular tissues.

**4.5 Alternative Boundary Conditions.** There are a variety of boundary conditions possible for biaxial testing. Among some recent publications, they can be roughly separated into clamped [13–17], cruciform [13,16,17,30–33], and tethered boundary condition [1,9–12]. Clamping, as previously mentioned, produces a drastically different and highly heterogeneous stress field. Moreover, the restriction to the lateral displacement of the edge essentially creates a stress shield for the ROI [13]. This effect increases in response to larger deformations, preventing direct estimation of the stress based on the forces applied to the boundary. Thus, inverse methods are necessary to estimate the stresses. In cruciform geometries, no matter whether the sample is tethered or clamped, this effect is reduced. However, in order to apply the proposed method, the effective sample dimension needs to be established due to its significance in the accuracy of the methods. It is not clear how the choice of cruciform geometry [13,16,17,30–33] impacts the effective specimen dimensions. Additionally, it is also not clear how the material will respond to shear. Shearing can be induced in a similar fashion to Sun et al. [2]. It is difficult to control and not straightforward to analyze for the cruciform geometry, as the transmission of forces along the extrusions will depend on the properties of the material. The forces applied to the central region may not be evenly distributed or even point in the same direction as the actuator. As such, cruciform geometries also require inverse methods to obtain accurate results.

Tethered setups do not restrict the deformation of the specimen, and can be made to distribute the forces evenly, avoiding similar problems with the other boundary conditions. For devices such as BioTester (cell scale), where one end of the tethers is fixed, the positions and thus the orientation of the tethers are easily defined based on the displacement of the actuators. Caution must be taken when there is no mechanism to ensure that the forces are evenly distributed; each tether will be loaded differently resulting in the tension being unevenly distributed. Moreover, when the tethers are rigidly attached and made of stiff materials (metal rods) such that they provide some resistance to bending, the large deformations and shear will also generate a bending moment that is difficult to account for in the stress analysis. This can impact both the stresses in the ROI and our ability to obtain accurate estimates of the stress. For systems with an equilibrating mechanism, a derivation is given in the Appendix. One might also note that, commonly, when the shear is minimal and the strain is not comparable to the length of the tethers, the symmetry of the system will mean that any of such errors are small to begin with. In the end, the most favorable setup is up to the investigator based on their specific intent and application.

**4.6 Implementation and Limitations.** This method can be easily implemented using readily available software package such as MATHEMATICA (Wolfram Research Corp.) or MATLAB (Mathworks, Inc.). Using MATHEMATICA with Gaussian quadrature for integration of moments, and conjugate gradient for optimization, and a solution is obtainable for a single protocol (~1500 points) within 3–10 s.

In the present approach, an assumption of homogeneous deformation is still necessary for calculating the tractions and specimen geometry. This simplifies the problem into one that is solvable in an analytical manner. As stated earlier, we feel that this is a reasonable approach to obtain the mechanical data for identifying the form and performing parameter estimation for any constitutive model. Additionally, the errors produced by this assumption are small and can be ignored. Once in place, such models and initial parameter estimates can be utilized in inverse modeling approaches for more complicated problems in functional tissues. Only a limited range of heterogeneities are considered in the model, but based on the accuracy of the results we believe that this is sufficient and should not be a significant factor. While non-square initial geometries are not considered in this paper, both preconditioning effects and anisotropy of the material model already produce a drastically different geometry than the idealized square and should be a much more significant factor.

**4.7 Summary.** We have developed a generalized method to determine stresses from the experimentally derived traction and testing geometry, as well as compensate for run-time inelastic effects by enforcing equilibrium using small rigid body rotations. Using FE simulations of the planar biaxial tests, we demonstrated that our method provides an improved method of calculating the resulting stresses under large shear and preconditioning effects. The effects of preconditioning and heterogeneities are properly accounted for in this model to produce a more accurate stress estimate, particularly for the shear stress. Larger errors are due to tether placement and specimen dimensions. We found that stress is mostly induced over the subregion bounded by the tethers, necessitating an adjustment to the specimen dimensions, and the tethers should be placed reasonably so that the forces are applied evenly along the whole edge. Overall, using the present corrections, more accurate models can be subsequently developed for soft tissue/biomaterial applications.

## Acknowledgment

This research was supported by NIH Grant Nos. HL-063026, HL-070969, and HL-108330.

## Nomenclature

- $a$  = area in the current state
- $A$  = area in the reference state
- $d\mathbf{l}$  = a line in the current state, used to represent the side of the specimen
- $d\mathbf{L}$  = a line in the reference state, used to represent the side of the specimen
- $\mathbf{E}$  = Green–Lagrange strain tensor
- $\mathbf{f}$  = force vector at each side
- $\mathbf{F}$  = deformation gradient
- $l$  = the length of the specimen in the current configuration
- $L$  = the length of the specimen in the initial referential configuration
- $\mathbf{M}$  = first moment
- $\mathbf{n}$  = normal to the side of the specimen in the current state
- $\mathbf{o}_Y$  = coordinate of the pivot between the two shafts of the lever system used by the actuators
- $\mathbf{P}$  = first Piola Kirchhoff stress
- $\mathbf{r}$  = position vector of point on the surface of the tissue
- $\mathbf{R}$  = rotation tensor
- $\mathbf{S}$  = second Piola Kirchhoff stress
- Bold = a vector or tensor quantity
- $\mathbf{t}$  = Cauchy stress
- $\mathbf{T}$  = traction vectors at each side
- $\mathbf{U}$  = right stretch tensor
- $\mathbf{v}^i$  = vectors representing the tethers used to exert force on the tissue
- $\mathbf{X}^i$  = coordinates of the attachment point of the tethers on the tissue
- $\mathbf{Y}^i$  = coordinate of the tangent points of the tether on the pulley shaft referenced to the pivot of the shafts  $\mathbf{o}$
- $\gamma$  = shear
- $\delta$  = the distance the shafts transverse during the experiment
- $\theta$  = the rigid body angle
- $\lambda$  = stretch
- $\varphi$  = the orientation angle of the shafts about their pivot  $\mathbf{o}_Y$
- $\Omega_r$  = the configuration of the specimen at the  $r$ th time point

## Subscripts

- $i$  = the component or a vector or tensor

## Superscripts

- $i$  = the  $i$ th coordinate or the  $i$ th vector, and is in fact not a component
- $(i)$  = that the scalar or vector quantity pertains to the side  $i$

## Appendix: Derivation of Traction Vectors for Self-Equilibrating Tethered Systems

**Device Geometry.** The traction vector should be determined based on the testing system. For devices such as BioTester (Cell Scale), where one end of the tethers is fixed, the orientation of the tethers is easier to determine. Self-equilibrating systems can be more complicated. Typical self-equilibrating tether systems involve wrapping tethers around a pulley with the ends attached to the specimen. For two-point attachment, only one pulley is involved. For four-point attachment, two pulleys are joined by a bar that can rotate about its midpoint [1]. The number of pulleys can be doubled for eight-point attachment, 16-point attachment, etc. In the case of two tethers, the system is constrained by the total length of the tether around the pulley which can be used to determine the displacement of the actuator. For every additional pulley added, a degree of freedom must be added representing the orientation of the bar joining it to the rest of the system. In all cases, the number of the constraints is equal to the number of degrees of freedom. We shall use the four-point attachment as an example, as it is the most commonly used number of tethers. We will assume the tethers are evenly spread (Fig. 1).

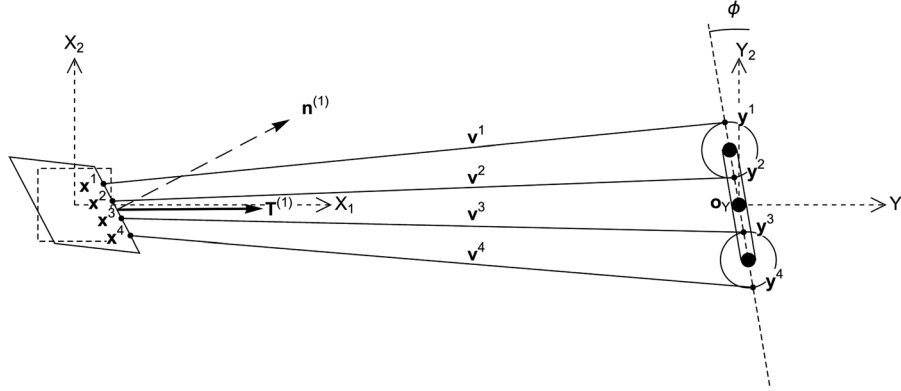


**Fig. 11 Close up of side 1 of the biaxial testing device under deformation of a specimen.** The normal vector  $\mathbf{n}$  and the average traction vector  $\mathbf{T}$  oriented at 0.85 deg and 7.6 deg are shown by the dashed arrows. The pulley system rotates about the pivot  $\mathbf{o}_Y$  by the angle  $\phi$ , and transverses along the test axis by the distance  $\delta$  (not shown). The tethers are represented by the vectors  $\mathbf{v}^i$ , which attach to the tissue at the points  $\mathbf{x}^i = \mathbf{F} \cdot \mathbf{X}^i$  and are tangent to the pulley shafts at the points  $\mathbf{y}^i = \mathbf{R}(\phi)\mathbf{Y}^i + \mathbf{o}_Y$ .

**Traction Orientation Vectors.** The general process for determining the orientation of the traction vectors is in three steps. (1) Determine the locations of orientation of the tethers in the initial unloaded state; this can be measured directly. (2) Determine the locations of the end of the tethers on the tissue using the deformation gradient. (3) Determine the remaining end of the tethers based on the constraints and mechanisms unique to that system. For devices such as BioTester (Cell Scale), step 3 is simple as the ends are fixed. The midpoint of the tethers on the specimen can be produced by the deformation gradient. The midpoint of the tether at the actuator only displaces with the actuator. The displacement of the actuator  $\delta$  can be measured directly, or determined using optimization by assuming the distance from the actuator and specimen remains constant, rather like how  $\delta$  is determined below. For our self-equilibrating example, we will denote the four tethers attached to the tissue using the vectors  $\mathbf{v}^1, \mathbf{v}^2, \mathbf{v}^3$ , and  $\mathbf{v}^4$ . The tether vectors  $\mathbf{v}^i$  are given by the difference between the tangent points on the shafts and the attachment points on the tissue. Let  $\mathbf{o}_Y$  be the pivot point of the lever system, which is moved along the experimental axis by the linear actuators. The position of  $\mathbf{o}_Y$  is indeterminate during the experiment.  $\mathbf{Y}^i$  are the position of tangent points on the shafts of the lever system relative to  $\mathbf{o}_Y$  in the initial free floating configuration. It is clear that the current coordinates of the tangent points on the shafts is simply  $\mathbf{R}(\phi)\mathbf{Y}^i + \mathbf{o}_Y$ , where  $\mathbf{R}(\phi)$  is a rotation matrix about  $\mathbf{o}_Y$  and  $\phi$  is the angle rotated to equilibrate the tension for all four tethers (Fig. 11). Furthermore, let  $\mathbf{X}^i$  be the four tether attachment points on the tissue in the initial free floating configuration. The current coordinates of the attachment points are simply determined using the overall deformation gradient  ${}^t_0\mathbf{F} = {}^t_1\mathbf{F}_0\mathbf{F}$ ,  $\mathbf{x} = {}^t_0\mathbf{F} \cdot \mathbf{X}$ . Thus the tether vectors,  $\mathbf{v}^i$ , are given by the difference

$$\mathbf{v}^i = (\mathbf{R}(\phi)\mathbf{Y}^i + \mathbf{o}_Y) - {}^t_0\mathbf{F} \cdot \mathbf{X}^i \quad (\text{A1})$$

The current pivot of the pulleys  $\mathbf{o}_Y(t)$  is not known during the experiment, and must be determined post hoc. However, note that the initial  $\mathbf{o}_Y(0)$  prior to any preconditioning and biaxial loading can always be measured. The current pivot  $\mathbf{o}_Y(t)$  at any time  $t$  is given by an additional distance moved by the actuators  $\delta$

$$\mathbf{o}_Y(t) = \mathbf{o}_Y(0) + \delta \mathbf{e}_1 \quad (\text{A2})$$

where  $\mathbf{e}_1$  be the unit vector in  $X_1$  direction. Thus we only need to find  $\phi$  and  $\delta$  to determine the complete experimental geometry of the system.

Note that  $\mathbf{v}^1$  and  $\mathbf{v}^2$  are part of the same tether and  $\mathbf{v}^3$  and  $\mathbf{v}^4$  are part of the same tether. Physically, for any loading condition, the tethers must remain taut and cannot stretch, so that  $|\mathbf{v}^1| + |\mathbf{v}^2|$  and  $|\mathbf{v}^3| + |\mathbf{v}^4|$  remain constant. Thus, for the current tether vectors  $\mathbf{v}^i(t)$ , given any  ${}^t_0\mathbf{F}$  and the initial free floating state tether vectors  $\mathbf{v}^i(0)$ , we can solve for  $\phi$  and  $\delta$  by requiring the sum of squares error (Eq. (A3)) to be minimized.

$$\text{SSE}(\phi, \delta) = ((|\mathbf{v}_1(t)| + |\mathbf{v}_2(t)|) - (|\mathbf{v}_1(0)| + |\mathbf{v}_2(0)|))^2 + ((|\mathbf{v}_3(t)| + |\mathbf{v}_4(t)|) - (|\mathbf{v}_3(0)| + |\mathbf{v}_4(0)|))^2 \quad (\text{A3})$$

Once the  $\mathbf{v}^i$  are known, the average tether vector  $\mathbf{v}^{\text{avg}}$  can be computed. In some cases, where the tethers are long enough such that they are essentially parallel with the test axes and do not rotate more than 5 deg during the test,  $\mathbf{v}^{\text{avg}}$  can simply be approximated to be a unit vector pointing along the axes without any loss of accuracy.

**Local Traction.** The total axial forces for each side is  $\mathbf{f} = f_1\mathbf{e}_1 + f_2\mathbf{e}_2$ , where  $f_1$  is the component along the  $X_1$  axis and  $f_2$  is component along the  $X_2$  axis. Often the axial forces are assumed to be aligned to the experimental axes. This is not true under shear and can produce significant differences and even reverse the sign of the shear stress. In the case, when the load cells are unidirectional, only the force along the axis  $f_1^{(1)}$  and  $f_2^{(2)}$  is measured. The off axis forces can be obtained by multiplying the on-axis force by the ratio of the components of the directional vector  $\mathbf{v}$ , i.e.,  $f_2 = f_1 v_2^{\text{avg}}/v_1^{\text{avg}}$ . The net traction vector  $\mathbf{T}$  is thus given by Eq. (8). The traction vectors for all other sides can be derived similarly.

## References

- [1] Sacks, M., 2000, "Biaxial Mechanical Evaluation of Planar Biological Materials," *J. Elast.*, **61**(1–3), pp. 199–246.
- [2] Sun, W., Sacks, M. S., Sellaro, T. L., Slaughter, W. S., and Scott, M. J., 2003, "Biaxial Mechanical Response of Bioprosthetic Heart Valve Biomaterials to High In-Plane Shear," *ASME J. Biomech. Eng.*, **125**(3), pp. 372–380.
- [3] Stella, J. A., Liao, J., and Sacks, M. S., 2007, "Time-Dependent Biaxial Mechanical Behavior of the Aortic Heart Valve Leaflet," *J. Biomech.*, **40**(14), pp. 3169–3177.
- [4] Sacks, M. S., 1999, "A Method for Planar Biaxial Mechanical Testing That Includes In-Plane Shear," *ASME J. Biomech. Eng.*, **121**(5), pp. 551–555.
- [5] Freed, A. D., Einstein, D. R., and Sacks, M. S., 2010, "Hypoelastic Soft Tissues: Part II: In-Plane Biaxial Experiments," *Acta Mech.*, **213**(1–2), pp. 205–222.
- [6] Fomovsky, G. M., and Holmes, J. W., 2010, "Evolution of Scar Structure, Mechanics, and Ventricular Function After Myocardial Infarction in the Rat," *Am. J. Physiol. Heart Circ. Physiol.*, **298**(1), pp. H221–228.



- [7] Sun, W., Sacks, M. S., and Scott, M. J., 2003, "Numerical Simulations of the Planar Biaxial Mechanical Behavior of Biological Materials," *ASME Summer Bioengineering*, L. J. Soslowsky, ed., ASME, Miami, FL, pp. 875–876.
- [8] Jor, J. W., Nash, M. P., Nielsen, P. M., and Hunter, P. J., 2011, "Estimating Material Parameters of a Structurally Based Constitutive Relation for Skin Mechanics," *Biomech. Model. Mechanobiol.*, **10**(5), pp. 767–778.
- [9] Bellini, C., Glass, P., Sitti, M., and Di Martino, E. S., 2011, "Biaxial Mechanical Modeling of the Small Intestine," *J. Mech. Behav. Biomed. Mater.*, **4**(8), pp. 1727–1740.
- [10] Azadani, A. N., Chitsaz, S., Matthews, P. B., Jaussaud, N., Leung, J., Tsinman, T., Ge, L., and Tseng, E. E., 2012, "Comparison of Mechanical Properties of Human Ascending Aorta and Aortic Sinuses," *Ann. Thorac. Surg.*, **93**(1), pp. 87–94.
- [11] Kamenskiy, A. V., Pipinos, I. I., Dzenis, Y. A., Lomneth, C. S., Kazmi, S. A. J., Phillips, N. Y., and MacTaggart, J. N., 2014, "Passive Biaxial Mechanical Properties and In Vivo Axial Pre-Stretch of the Diseased Human Femoropopliteal and Tibial Arteries," *Acta Biomater.*, **10**(3), pp. 1301–1313.
- [12] Gregory, D. E., and Callaghan, J. P., 2011, "A Comparison of Uniaxial and Biaxial Mechanical Properties of the Annulus Fibrosus: A Porcine Model," *ASME J. Biomech. Eng.*, **133**(2), p. 024503.
- [13] Sun, W., Sacks, M. S., and Scott, M. J., 2005, "Effects of Boundary Conditions on the Estimation of the Planar Biaxial Mechanical Properties of Soft Tissues," *ASME J. Biomech. Eng.*, **127**(4), pp. 709–715.
- [14] O'Connell, G., Sen, S., and Elliott, D., 2012, "Human Annulus Fibrosus Material Properties From Biaxial Testing and Constitutive Modeling Are Altered With Degeneration," *Biomech. Model. Mechanobiol.*, **11**(3–4), pp. 493–503.
- [15] Sommer, G., Eder, M., Kovacs, L., Pathak, H., Bonitz, L., Mueller, C., Regitnig, P., and Holzapfel, G. A., 2013, "Multiaxial Mechanical Properties and Constitutive Modeling of Human Adipose Tissue: A Basis for Preoperative Simulations in Plastic and Reconstructive Surgery," *Acta Biomater.*, **9**(11), pp. 9036–9048.
- [16] Hu, J. J., Chen, G. W., Liu, Y. C., and Hsu, S. S., 2014, "Influence of Specimen Geometry on the Estimation of the Planar Biaxial Mechanical Properties of Cruciform Specimens," *Exp. Mech.*, **54**(4), pp. 615–631.
- [17] Simón-Allué, R., Cordero, A., and Peña, E., 2014, "Unraveling the Effect of Boundary Conditions and Strain Monitoring on Estimation of the Constitutive Parameters of Elastic Membranes by Biaxial Tests," *Mech. Res. Commun.*, **57**(0), pp. 82–89.
- [18] Lanir, Y., 1979, "A Structural Theory for the Homogeneous Biaxial Stress-Strain Relationships in Flat Collagenous Tissues," *J. Biomech.*, **12**(6), pp. 423–436.
- [19] Lanir, Y., and Fung, Y. C., 1974, "Two-Dimensional Mechanical Properties of Rabbit Skin. II. Experimental Results," *J. Biomech.*, **7**(2), pp. 171–182.
- [20] Fan, R., and Sacks, M. S., 2014, "Simulation of Planar Soft Tissues Using a Structural Constitutive Model: Finite Element Implementation and Validation," *J. Biomech.*, **47**(9), pp. 2043–2054.
- [21] Sacks, M. S., 2000, "A Structural Constitutive Model for Chemically Treated Planar Connective Tissues Under Biaxial Loading," *Comput. Mech.*, **26**(3), pp. 243–249.
- [22] Sacks, M. S., Lam, T. V., and Mayer, J. E. Jr., 2004, "A Structural Constitutive Model for the Native Pulmonary Valve," 26th Annual International Conference of the IEEE Engineering in Medicine and Biology Society (IEMBS), San Francisco, CA, Sept. 1–5, Vol. 2, pp. 3734–3736.
- [23] Sacks, M. S., Merryman, W. D., and Schmidt, D. E., 2009, "On the Biomechanics of Heart Valve Function," *J. Biomech.*, **42**(12), pp. 1804–1824.
- [24] Lee, C. H., Amini, R., Gorman, R. C., Gorman, J. H., III, and Sacks, M. S., 2014, "An Inverse Modeling Approach for Stress Estimation in Mitral Valve Anterior Leaflet Valvuloplasty for In-Vivo Valvular Biomaterial Assessment," *J. Biomech.*, **47**(9), pp. 2055–2063.
- [25] Billiar, K. L., and Sacks, M. S., 2000, "Biaxial Mechanical Properties of the Natural and Glutaraldehyde Treated Aortic Valve Cusp—Part I: Experimental Results," *ASME J. Biomech. Eng.*, **122**(1), pp. 23–30.
- [26] Billiar, K. L., and Sacks, M. S., 2000, "Biaxial Mechanical Properties of the Native and Glutaraldehyde-Treated Aortic Valve Cusp: Part II—A Structural Constitutive Model," *ASME J. Biomech. Eng.*, **122**(4), pp. 327–335.
- [27] Sacks, M. S., Hamamoto, H., Connolly, J. M., Gorman, R. C., Gorman, J. H., III, and Levy, R. J., 2007, "In Vivo Biomechanical Assessment of Triglycidyl-amine Crosslinked Pericardium," *Biomaterials*, **28**(35), pp. 5390–5398.
- [28] Sun, W., and Sacks, M. S., 2005, "Finite Element Implementation of a Generalized Fung-Elastic Constitutive Model for Planar Soft Tissues," *Biomech. Model. Mechanobiol.*, **4**(2–3), pp. 190–199.
- [29] Fung, Y. C., 1993, *Biomechanics: Mechanical Properties of Living Tissues*, Springer Verlag, New York.
- [30] Hanabusa, Y., Takizawa, H., and Kuwabara, T., 2013, "Numerical Verification of a Biaxial Tensile Test Method Using a Cruciform Specimen," *J. Mater. Process. Technol.*, **213**(6), pp. 961–970.
- [31] Zhao, X., Berwick, Z. C., Krieger, J. F., Chen, H., Chambers, S., and Kassab, G. S., 2014, "Novel Design of Cruciform Specimens for Planar Biaxial Testing of Soft Materials," *Exp. Mech.*, **54**(3), pp. 343–356.
- [32] Ramault, C., Makris, A., Van Hemelrijck, D., Lamkanfi, E., and Van Paepegem, W., 2011, "Comparison of Different Techniques for Strain Monitoring of a Biaxially Loaded Cruciform Specimen," *Strain*, **47**, pp. 210–217.
- [33] Makris, A., Vandenbergh, T., Ramault, C., Van Hemelrijck, D., Lamkanfi, E., and Van Paepegem, W., 2010, "Shape Optimisation of a Biaxially Loaded Cruciform Specimen," *Polym. Test.*, **29**(2), pp. 216–223.